Inorganic Chemistry

Article

Elucidating the Effects of the Composition on Hydrogen Sorption in TiVZrNbHf-Based High-Entropy Alloys

Gustav Ek,* Magnus M. Nygård, Adriano F. Pavan, Jorge Montero, Paul F. Henry, Magnus H. Sørby, Matthew Witman, Vitalie Stavila, Claudia Zlotea, Bjørn C. Hauback, and Martin Sahlberg

Read Online

ACCESS | Metrics & More | Article Recommendations | Supporting Information

ABSTRACT: A number of high-entropy alloys (HEAs) in the TiVZrNbHf system have been synthesized by arc melting and systematically evaluated for their hydrogen sorption characteristics. A total of 21 alloys with varying elemental compositions were investigated, and 17 of them form body-centered-cubic (bcc) solid solutions in the as-cast state. A total of 15 alloys form either face-centered-cubic (fcc) or body-centered-tetragonal (bct) hydrides after exposure to gaseous hydrogen with hydrogen per metal ratios (H/M) as high as 2.0. Linear trends are observed between the volumetric expansion per metal atom $[(V/Z)_{fcc/bct} - (V/Z)_{bcc/hcp}]/(V/Z)_{bcc/hcp}$ with the valence electron concentration and average Pauling electronegativity (χ_p) of the alloys. However, no correlation was observed between the atomic size mismatch, δ, and any investigated hydrogen sorption property such as the maximum storage capacity or onset temperature for hydrogen release.
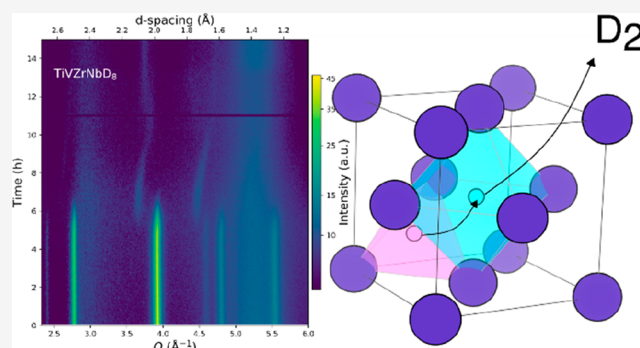
INTRODUCTION

Today's society faces a number of challenges in order to switch the large-scale energy production from fossil fuels to renewable energy sources. One of these is the inherent fluctuations in the grid during peak hours when using wind and solar energy sources, requiring large-scale energy storage. Hydrogen is considered to be one of the most attractive solutions for this purpose because of its large gravimetric energy density. However, handling and storing compressed hydrogen gas comes with several engineering challenges as well as the high cost of compressing hydrogen. Instead, hydrogen can be stored in the solid state using a metal hydride, which offers improved safety and higher volumetric energy densities.[1] Many intermetallic compounds have been tested over the years for this purpose such as alloys of the type AB$_2$, AB$_5$, TiFe, and body-centered-cubic (bcc), for instance, TiV. Unfortunately, all of these systems have drawbacks, such as phase separation after repeated hydrogen cycling, extensive surface passivation, and/or poor sorption kinetics.[2−4]

An unconventional alloying strategy was proposed by Yeh et al.[5] in which typically four or more elements in nearly equimolar concentrations are mixed. These kinds of alloys usually crystallize in simple structures such as bcc, cubic close-packed, or hexagonal close-packed (hcp). It is believed that these structures are stabilized because of the high entropy of mixing, ΔS_{mix}, caused by the large number elements occupying the same crystallographic site in the structure. This, in turn, has given rise to the name high-entropy alloys (HEAs). HEAs have attracted

significant attention because of some excellent properties in terms of the tensile strength, magnetism, and superconductivity.[6,7]

Some reports have also emerged investigating the hydrogen sorption properties in these kinds of systems.[8−20] For instance, it has been reported that TiVZrNbHf HEA was able to absorb large amounts of hydrogen, reaching a H/M ratio of 2.5,[14] which is greater than any of the five constituent elements. Such high H/M ratios are not usually observed for transition metals unless under extreme pressures of 5 GPa in TiH$_{1.8+\gamma}$.[21] The behavior of TiVZrNbHf is closer to that of rare-earth (RE) metal hydrides, such as CeH$_x$. In this case, both the octahedral and tetrahedral interstitial sites in the REH$_x$ fluorite structure are significantly occupied so that the H/M ratio can be as high as 3.[22] It has been suggested that the size mismatch of the constituent elements could facilitate significant hydrogen occupation at both sets in TiVZrNbHf.[14] The atomic size mismatch is often quantified by the δ parameter:
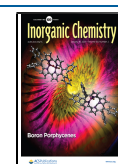
Table 1. Comparison of Unit Cell Parameters a, Manometric Hydrogen Capacity H/M, Valence Electron Concentration VEC, Atomic Size Mismatch δ, Mean Pauling Electronegativity χ_p, and Unit Cell Expansion per Metal Atom α for All Investigated Alloys and Their Corresponding Hydrides

composition	a_{bcc} (Å)	$a_{bcc/bct}$ (Å)	c_{bct} (Å)	H/M	VEC	δ (%)	χ_p	α
TiVZrNbHf	3.3634(8)	4.5783(7)		1.99	4.40	5.72	1.48	0.26
TiVZrNbHf$_{0.5}$	3.34214(0)	4.5620(5)		2.00	4.44	5.80	1.50	0.27
TiVZrNb	3.3047(8)	4.5385(1)		1.98	4.50	5.81	1.53	0.30
TiVZr$_{0.5}$NbHf	3.3239(5)	4.5539(2)		1.99	4.44	5.54	1.50	0.29
TiVNbHf	3.2976(7)	4.5202(7)		1.99	4.50	5.12	1.52	0.29
TiVZrNb$_{0.5}$Hf	3.3681(5)	3.2471(2)	4.5731(8)	1.82	4.33	6.02	1.47	0.26
TiVZrHf	3.3809(0)				4.25	6.37	1.45	
TiV$_{0.5}$ZrNbHf	3.3911(3)	4.6114(3)		1.96	4.33	5.07	1.46	0.26
TiZrNbHf	3.4270(5)	3.2780(2)	4.6714(3)	1.98	4.25	3.82	1.44	0.25
Ti$_{0.5}$ZrNbHf	3.3665(5)	4.5962(2)		1.97	4.44	5.96	1.47	0.27
VZrNbHf	3.3943(9)				4.50	6.22	1.47	
TiVNb	3.1867(7)	4.4375(3)		1.96	4.67	3.76	1.59	0.35
TiVZr					4.33	6.71	1.50	
TiVHf	3.2966(4)	3.1933(9)	4.4789(7)	1.98	4.33	5.89	1.49	0.27
TiZrNb	3.3884(6)	4.6161(9)		1.86	4.33	4.06	1.49	0.26
TiNbHf	3.3799(8)	4.5904(2)		2.00	4.33	3.16	1.48	0.25
TiZrHf	hexagonal	3.3835(8)	4.4566(7)	2.00	4.00	3.93	1.39	0.21
VZrNb					4.67	6.65	1.52	
VNbHf	3.3137(9)				4.67	5.88	1.51	
VZrHf					4.33	7.10	1.42	
ZrNbHf	3.4758(1)	4.6970(0)		2.00	4.33	3.18	1.41	0.23

$$\delta = \sqrt{\sum_{i=1}^{N} c_i \left(1 - \frac{r_i}{\bar{r}}\right)^2} \times 100\%$$

where c_i and r_i are the atomic fraction and radius of element i, respectively, and $\bar{r}$ is the average atomic radius of the alloy consisting of N different elements. To investigate the above-mentioned hypothesis, Zlotea et al. studied the hydrogen storage properties of TiZrNbHfTa.[16] In this HEA, the atomic size mismatch is reduced to $\delta = 4.01\%$ from $\delta = 6.08\%$ in TiVZrNbHf by substituting the smallest element V by Ta. It was found that this caused the alloy to behave more like V, with a two-step hydrogen sorption reaction reaching a maximum H/M ratio of 2.[22] A more systematic study was performed by Nygård et al. in which metal hydrides formed from bcc HEAs with the compositions TiVZr$_x$NbTa$_{1-x}$ ($0 \leq x \leq 1$) and TiVZr$_{1+x}$Nb ($1 \leq x \leq 2$).[17] These HEAs have δ in the range 3.53–6.34%, but the maximal H/M ratios were all around 2.0 despite the fact that several systems have δ values comparable to that of TiVZrNbHf. Nygård et al. followed up on another study investigating trends between the hydrogen storage properties and valence electron concentration (VEC) of the HEA, which is defined as

$$\text{VEC} = \sum_{i=1}^{N} c_i \text{VEC}_i$$

where c_i and VEC_i are the atomic fraction and number of valence electrons of the N different element in the HEA. Two trends were found to correlate well with VEC: first, the volumetric expansion per metal atom, $\alpha = [(V/Z)_{fcc/bct} - (V/Z)_{bcc/hcp}]/(V/Z)_{bcc/hcp}$ (fcc = face-centered cubic; bct = body-centered tetragonal), increases linearly with VEC; second, the onset temperature of hydrogen desorption decreases linearly with increasing VEC, enabling an onset at room temperature (RT) if extrapolated to VEC = 6.40. This destabilization mechanism could potentially allow for determination of the compositions a priori with targeted hydrogen sorption properties for a selected

application, overcoming some of the current drawbacks with the several classes of metal hydrides mentioned above.

In a recently published study by Nygård et al., it was shown by total scattering that deuterium occupies both the tetrahedral and octahedral sites in TiVZrNbHfD$_{10}$. This finding supports the assumption that hydrogen (deuterium) will occupy different interstitial sites in certain HEAs.[23]

In this study, we further investigate the origin of the high H/M ratios observed in the TiVZrNbHf HEA by varying the elemental composition and thereby the local metal–hydrogen coordination. In total, 21 alloys with compositions related to TiVZrNbHf are investigated. The compositions were obtained by removing one and/or two metals successively to the quaternary and ternary counterparts (Table 1). This, in turn, produces alloys with a wide range of values such as δ (3.16–7.10%), VEC (4.00–4.67), and average Pauling electronegativity (χ_p; 1.41–1.59). In the present work, the atomic radii, VECs, and χ_p values are taken from ref 24.

◼ EXPERIMENTAL SECTION

As-cast samples were prepared by arc-melting stoichiometric amounts of the constituent metals: Ti (Kurt J. Lesker, 99.995% metals basis), V (ChemPur 99.9% metals basis), Zr (ChemPur, 99.8% metals basis excluding Hf), Nb (Alfa Aesar, 99.5% metals basis), and Hf (ChemPur, 99.8% metals basis excluding Zr) in an Ar atmosphere. Prior to melting, the chamber was purified of O$_2$ contamination by melting a Ti oxygen-getter piece. The samples were remelted five times and flipped between each melting to improve their chemical homogeneity. Weight loss after synthesis was in all cases less than 0.1 wt %, and the composition can therefore be considered to be close to the nominal. After synthesis, small quantities were filed into a coarse powder for diffraction analysis. The remaining ingot was then cut and put into an in-house-built Sieverts-type apparatus[25] for hydrogenation. Most samples were activated at 340 °C for 2 h in a dynamic vacuum and subsequently cooled to RT before hydrogen exposure. TiZrNbHf, TiZrNb, TiNbHf, TiZrHf, and ZrNbHf showed very slow absorption kinetics and required activation at 500 °C in a dynamic vacuum, followed by hydrogen exposure at 300 °C. After activation, the samples were

exposed to a hydrogen pressure of 40 ± 3 bar in a single pulse. The samples were then left under these conditions until the change in pressure was below the detectable limits of the pressure transducer (±0.3 bar). After hydrogenation, all samples could be easily crushed and ground into a fine powder using an agate mortar. The samples for the neutron diffraction experiments were prepared by a similar route of synthesis but with deuterium gas (Air Liquide, 99.7%) instead of hydrogen to reduce the incoherent scattering from the sample. Sample handling of synthesized metal hydrides was done in an Ar-filled glovebox with O_2 and H_2O levels below 1 ppm.

Powder X-ray diffraction was conducted on a Bruker D8 Advance diffractometer using Cu Kα radiation in the Bragg–Brentano geometry on zero-background silicon holders. Data were analyzed using the Rietveld method implemented in the software *Topas 6 Academic*.[26,27] In a typical refinement, the background was fitted as a fifth-order Chebyshev polynomial and the peaks by a Thompson–Cox–Hastings pseudo-Voigt function. The site occupancies of metals were fixed to the nominal composition in all cases.

Thermal gravimetric analysis (TGA) and differential scanning calorimetry (DSC) were conducted simultaneously in a Netzsch STA 449 F1 Jupiter apparatus equipped with a SiC furnace. Samples were loaded into alumina crucibles and heated at 2, 5, 10, and 20 °C/min to 1000 °C under an Ar flow of 50 mL/min for Kissinger analysis. The samples were briefly exposed to air during loading into the apparatus.

In situ neutron powder diffraction data were collected at the Polaris diffractometer[28] at the ISIS Neutron and Muon source using the Intelligent Gravimetric Analyzer for Neutrons (IGA^n, Hiden Isochema) described previously.[29] The sample powders were loaded into a quartz bucket, which was then hung from a fine-tungsten wire connected to the balance. Because of the low-neutron-scattering cross section of the alloys, a quartz tube was used as an outsert instead of stainless steel. The setup was heated by two furnace elements located above and below the sample bucket at a heating rate of 1 °C/min up to a maximum of 500 °C with a thermocouple situated above the bucket. To prevent heat loss into the diffractometer tank, a heat shield made out of V-sheet metal was placed around the quartz tube. Because of the low signal-to-noise ratio, every 10th data set had to be averaged, resulting in a time resolution of approximately 23 min.

Pressure composition isotherms (PCIs) were collected using a Setaram PCTPro system. Samples were loaded into airtight stainless-steel vessels, connected to the system, and put under a vacuum before thermal activation. The thermocouple measuring the temperature is located outside the stainless-steel pressure vessel in a thermocouple well to minimize the thermal gradients between the samples and vessel exterior. The pressure transducers had an accuracy of ±1%. The PCT experiments were conducted isothermally after thermal activation. The measurement had to be carried out at relatively high temperatures to ensure that the kinetics of hydrogen uptake were fast enough to reach equilibrium. All measurements were conducted in the Δp mode, using an increasing pressure step starting at Δp = 0.1 bar of hydrogen.

The enthalpy and entropy of hydrogenation were determined using a hybrid PCT/van't Hoff method. The method consists of determining the equilibrium pressure p_1 of a sample at a temperature T_1 by measuring a full isotherm, then heating the sample to temperature T_2, pressurizing the sample with hydrogen, and letting the system come to chemical equilibrium over time at a constant temperature. The equilibrium pressure p_2 is recorded when no further changes in pressure occur. The method works best when prior information exists about the thermodynamics and approximate ΔH and ΔS values of the metal hydride.[15] In addition, because the H/M ratio can vary with temperature, it is important to first measure a full hydrogen isotherm to ensure that the plateau region is relatively flat. The hydrogen equilibrium pressure P_{eq} and temperature are determined by the thermodynamic parameters of the system, as described by the van't Hoff equation:

$$\ln\left(\frac{P_{eq}}{P_0}\right) = -\frac{\Delta H}{RT} + \frac{\Delta S}{R}$$

where P_0 and R represent the standard atmospheric pressure and universal gas constant, respectively. Because the van't Hoff thermodynamic relationship dictates that changing the temperature of the sample induces a commensurate change in the equilibrium pressure in the system, the as-measured equilibrium pressures from the direct van't Hoff method[30] can be used to estimate the ΔH and ΔS values and is particularly useful for materials displaying sluggish kinetics, for which measurement of the isotherms at a number of various temperatures is impractical.

RESULTS AND DISCUSSION

Synthesis of Alloys and Hydrides. A selection of properties for the investigated alloys and their corresponding hydrides are summarized in Table 1. The X-ray diffraction patterns before and after hydrogenation presented in Figure 1
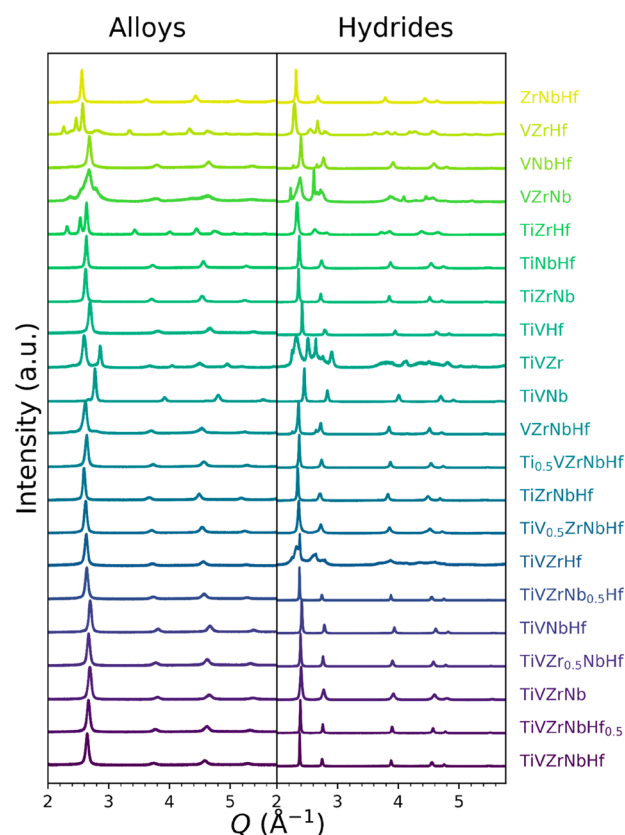

Figure 1. Powder X-ray diffraction patterns of the as-synthesized alloys and their corresponding hydrides.

show that most of the as-cast alloys can be indexed with a bcc lattice ($Im\overline{3}m$) with a few exceptions. TiVZr crystallizes in two bcc phases with the unit cell parameters a_1 = 3.4263(4) Å and a_2 = 3.1065(2) Å, respectively. TiZrHf assumes a hcp ($P6_3/mmc$) structure with a = 3.1513(5) Å and c = 4.9632(9) Å, which is similar to previous findings.[31] The presence of a hexagonal solid solution phase is interesting because it is scarcely found in the literature.[6] Usually, most hcp HEAs found so far require RE metals or transition metals at extreme pressures.[32,33] VZrNbHf, VZrHf, and VZrNb show diffraction peaks other than those that can be indexed in a bcc lattice, indicating the formation of other intermetallic phases. No attempts were made to characterize the composition or crystallographic structures of these additional phases because they are not to be classified as single-phase solid solution HEAs.

Once hydrogenated, most of the alloys form fcc hydrides ($Fm\overline{3}m$), while TiVZrNb$_{0.5}$Hf, TiZrNbHf, TiVHf, and TiZrHf form bct ones ($I\frac{4}{m}mm$). No clear way to predict what alloys would form bct hydrides instead of fcc was found with any of the considered parameters (δ, VEC, and χ_p). However, it is known that Zr and Hf tend to form bct metal hydrides at higher hydrogen concentrations.[34] All of the alloys that were found to form bct metal hydrides in this study have high concentrations of these elements. The multiphase alloys mentioned above also produce multiphase metal hydrides. Moreover, TiVZrHf, VZrNbHf, and VNbHf phase-separate during hydrogenation. This may be induced by heating during the activation procedure, indicating poor thermal stability or hydrogen-induced phase separation.

The maximum hydrogen storage capacities that were measured manometrically for the metal hydrides are presented in Figure 2. As can be seen, the metal hydrides have capacities
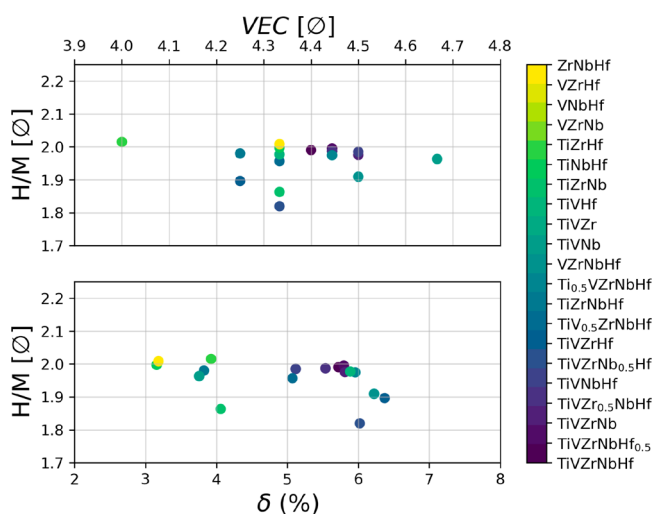

Figure 2. Maximum H/M of investigated alloys as a function of the VEC (top) and δ (bottom).

close to, but not exceeding, H/M = 2 within experimental error. Similar to the work by Nygård et al., no trends can be seen between the storage capacities and atomic size mismatch of the alloys that were suggested as the explanation for the high H/M found in TiVZrNbHf.[14,17] Furthermore, the H/M of 2.5 observed in TiVZrNbHf from ref 14 could not be replicated in the current setup. While the maximum hydrogen contents are similar, the hydrogen absorption characteristics of the investigated metal hydrides are greatly different. Most systems will absorb at RT after activation at 340 °C and reach full capacity within a few hours after hydrogen exposure (Figure S1). However, the behavior changes once V is partially or completely removed. TiV$_{0.5}$ZrNbHf will still absorb under the same conditions, but the kinetics are extremely slow and only reach H/M of 1.3 even if left under hydrogen pressure for several days. Complete removal of V requires activation at 500 °C and hydrogenation at elevated temperatures (Figure S1). To fully understand the role of V on the activation procedure would require an additional detailed surface study that is outside the scope of this work.

Similar to the work of Nygård et al.,[18] expansion of the unit cell volume per metal atom from the alloy to the hydride phase, α, follows a linear trend in both VEC and χ_p (Figure 3).
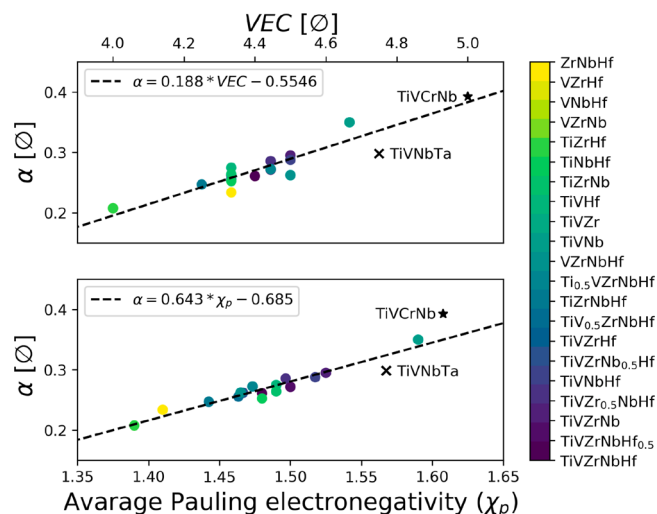

Figure 3. Volumetric unit cell expansion per metal atom ($\alpha = [(V/Z)_{\text{fcc/bct}} - (V/Z)_{\text{bcc/hcp}}]/(V/Z)_{\text{bcc/hcp}}$) upon hydrogenation as a function of the VEC (top) and χ_p (bottom).

Interestingly, the trend is still valid, even though some systems have different crystal structures with different packing factors, such as 0.64 (bcc) and 0.74 (hcp). Reference 18 showed that TiVNbTa and TiVCrNb were slight outliers to the trend, giving smaller and larger than expected expansions, respectively. This behavior is the same when looking at χ_p in Figure 3.

The difference in unit cell expansion upon hydrogen incorporation is surprising because the hydrogen concentrations are similar in all of the considered alloy systems. It is well established that hydrogen causes a constant volume expansion of 2.8 ± 0.2 Å^3 in d-band metals[22] because of hybridization of H 1s and metal d orbitals. However, in lanthanide metals, volume contraction can occur because of electronic structural changes from metallic to semiconductive or very large unit cell expansions such as in CeRn$_2$. It could be that HEAs behave more like lanthanides in their hydrogen-induced structural changes than d metals, which was also suggested in earlier works on TiVZrNbHf.[14] To fully understand the electronic configurations of these hydride systems will require more detailed theoretical work that is outside the scope of this work.

Thermal Analysis. Owing to their great chemical tunability, the hydrogen release mechanisms of HEA-based metal hydrides have shown significant complexity.[17,18] Simple substitution of just one element has, for instance, shown a change from a single step to a two-step hydrogen release mechanism when V is substituted for Ta in TiVZrNbHfH$_x$.[16] A summary of the TGA/DSC measurements for the 15 systems that produced single-phase hydrides can be found in Figure S2. The simplest system is TiVNbH$_x$, which has a single desorption event upon going from a dihydride to the hydrogen-free bcc alloy. In all other systems, hydrogen is released in at least two steps. Nygård et al. proposed these steps to be first a transition from the fcc dihydride to an intermediate bcc monohydride, followed by further release to the hydrogen-free alloy.[18] This is also seen in most of these systems, although some have additional endothermic peaks in the DSC signal associated with mass loss, where we also see contributions from yet another intermediate solid solution α phase. TiVZrNbHfH$_x$, which has been described to have both a single step and a two-step desorption mechanism, shows a rather interesting behavior, where the first DSC peak is split in two. This could indicate release from one preferential hydrogen

interstitial before the other if both are being occupied simultaneously, as has been suggested in the literature.[14,15,23] The most peculiar DSC signal seen in all systems belongs to TiZrHfH$_x$, where it is the third event that gives the sharpest DSC signal. Notable in all measurements is that the samples are highly prone to oxidation (even under very pure conditions) and start to gain mass as soon as the hydrogen release is finished. Therefore, mass gain during the main desorption cannot be excluded and makes the interpretation of quantities like the gravimetric hydrogen content unreliable, especially for slower heating rates. TiZrHfH$_x$ for instance, has a gravimetric estimate of 0.83 wt % H$_2$ if heated at 2 K/min and 1.59 wt % H$_2$ at 20 K/min. In this extreme case, the mass gain flattens the DSC curve during the first desorption event at heating rates of 2 and 5 K/min, making determinations of the onset temperatures impossible (it is therefore not present in the Kissinger analysis in Figure S3).

Figure 4 shows the onset temperature of desorption for the first and second events as a function of the VEC taken from the
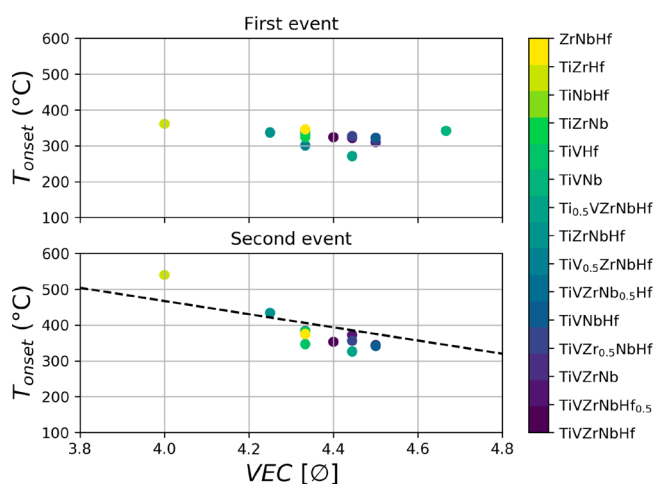

Figure 5. Activation energies, E_a, for the first and second desorption events as determined by Kissinger analysis of DSC measurements during desorption. The two events are plotted as a function of the VEC and χ_p in the top and bottom parts, respectively. The corresponding Kissinger plots can be found in Figure S3.

all investigated hydrides, and no systematic variations were found with respect to either VEC, χ_p, or δ.

Neutron Diffraction. To shed light on the nature of the desorption behavior in these systems, in situ neutron diffraction coupled with simultaneous gravimetric measurements were conducted for three selected samples with increasing compositional complexity, starting with TiVNb and subsequently adding Zr and Hf. These results are presented in Figure 6. Because the neutron scattering cross section is very weak in the deuterium-free alloys (for example, 45 times greater in TiVNbD$_6$ than in TiVNb, as can be seen in Table S1), information on the deuterium content from the gravimetric measurement needed to be fed into the Rietveld refinements; otherwise, the occupancy factors would refine to maximum.

Similar to previous results, TiVNbD$_6$ has deuterium situated solely in the tetrahedral interstitial site of the fcc lattice,[23] with the exception that in this case the site is fully occupied with deuterium. The deuterium in this system is gradually released from the tetrahedral sites in a single step, as indicated by the refined deuterium occupancy from sequential Rietveld refinements, as shown in Figure 6a. At around 360 °C, the diffraction lines from the fcc phase disappear at a deuterium occupancy of 0.54 (D/M = 1.08), which appears to be the lower solubility limit. After this transition, the gravimetric data still indicate that deuterium is left in the sample; however, it is clearly not detectable by diffraction, as no new additional Bragg peaks appear. The reason for this could be that the α phase is heavily disordered and deuterium has no fixed site or that the signal is not strong enough. Figure S5 shows simulated neutron powder diffraction patterns as a function of the deuterium content. Looking at the lower panels in Figure S5 of a desorbed bcc phase with D/M $\leq$ 1 in an octahedral interstitial site (occ(D^{oct}) $\leq \frac{1}{3}$), it is clear that nearly all intensity is gone, with only the (110) reflection being visible. The data do, however, not show any visible reflections, most likely because of the low average scattering length on the metal site (1.07 fm).

TiVZrNbD$_8$ shows a more complex desorption behavior. In this case, new diffraction lines are indeed appearing around 295 °C that can be indexed in a bcc lattice. From the refined deuterium occupancies to the right of Figure 6b), there seems to

Figure 4. Onset temperature of hydrogen desorption from the investigated HEA-based hydrides. The onset temperature for the first and second events are shown in the upper and lower parts, respectively. The linear trend between the VEC and T_{onset} found by Nygård et al. is shown for reference (reproduced with permission from ref 18. Copyright 2019 Elsevier).

10 °C/min desorption measurements. As can be seen, the onset for the first event stays at a rather constant temperature in the range of 300−340 °C, while the second event decreases with increasing VEC. The trend is similar to, but does not follow precisely, the one proposed in ref 18, where in this case, the data yield a more negative correlation. The biggest outlier is once again TiZrHfH$_x$, where the second event takes place about 100 °C higher than the other hydrides. As discussed above, this is also not even the main desorption event for TiZrHfH$_x$, which is the third event with a T_{onset} of 657 °C. A corresponding plot of Figure 4 against the mean χ_p showed no trends and can be found in Figure S4.

The series of Kissinger analyses shown in Figure 5 were carried out on the first and second desorption events. Similar to ref 18, the activation energy of TiVNbH$_x$ is the largest for the first event. The other ternary systems have lower activation energies, indicating that not only the amount of principal elements or chemical composition in the alloy dictates the kinetics. The activation energy for the second event is similar for
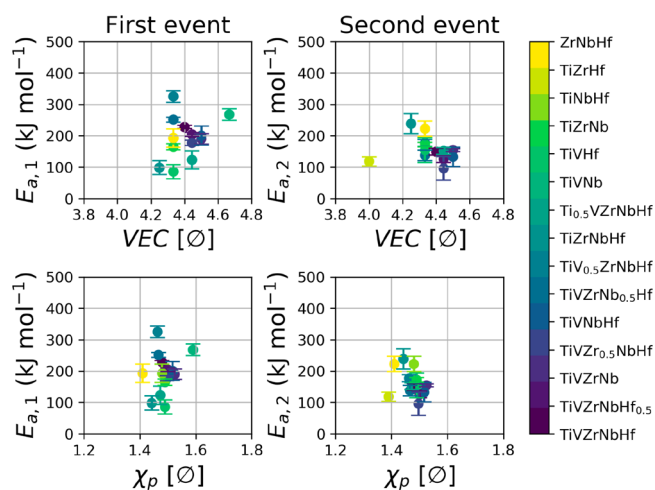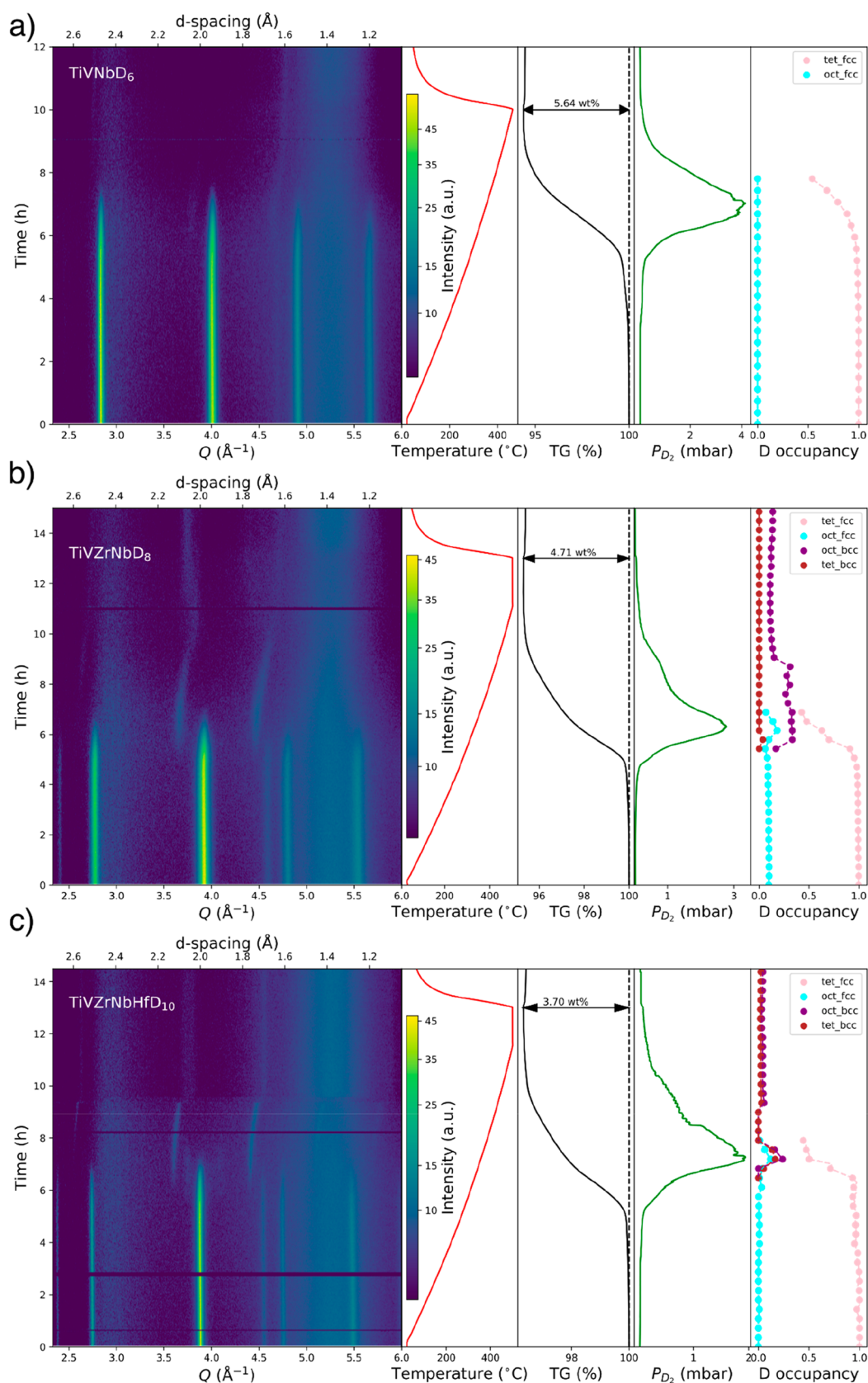
Figure 6. Simultaneous neutron diffraction and gravimetric analysis during desorption of (a) TiVNbD$_6$, (b) TiVZrNbD$_8$, and (c) TiVZrNbHfD$_{10}$. The neutron diffraction data shown are from the backscattering bank of Polaris (larger versions can be found in Figures S6–S8).

be both desorption of deuterium from the tetrahedral site and a jump to unoccupied octahedral sites that are then later desorbed.

It has been suggested in ref 23 that interstitial sites with a higher average VEC on the local surrounding metal atoms would leave

first, which could also potentially be the case here because there are more sites with lower VEC available with the introduction of Zr compared to TiVNb. The mechanism could therefore be that deuterium jumps from a higher-VEC tetrahedral site to a lower-VEC octahedral site during desorption. This kind of information is, however, not possible to extract from these data. In the bcc phase, deuterium is seen to preferentially occupy the octahedral interstitial site.

The desorption of $TiVZrNbHfD_{10}$ looks overall quite similar to that of $TiVZrNbD_8$. The main difference is that deuterium initially occupies both interstitials in the bcc phase, with a slight preference toward the octahedral. Our data indicate that deuterium is desorbed preferentially from the octahedral bcc sites at this stage of the reaction. Quantative information about the deuterium occupancy is difficult to extract, however, because of the low diffraction signal. It is apparent from Figure S5 that deuterium preferably sits at the octahedral interstitial because the relative intensities of the (200) and (211) reflections are comparable.

Common for all three samples is that the maximum deuterium capacity measured gravimetrically after the synthesis (6.26, 5.64, and 4.33 wt % of 1.99, 1.98, and 1.98 D/M for $TiVNbD_6$, $TiVZrNbD_8$, and $TiVZrNbHfD_{10}$, respectively) is never desorbed because we are limited to a maximum temperature of 500 °C of the experimental setup. It has been shown in the literature by in situ X-ray diffraction that $TiVZrNbH_x$ requires temperatures of up to 800 °C for full desorption, where the bcc phase would eventually split into two bcc phases.[17] No such behavior was observed in this work.

PCIs. The measured PCI curves are shown in Figure 7 and display a single hydrogen absorption plateau for three alloy
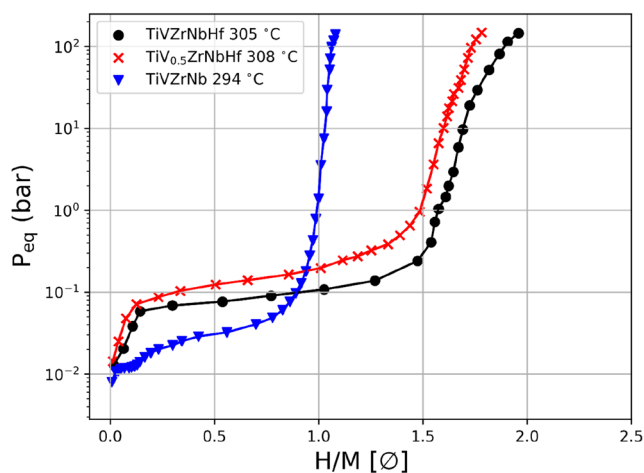

Figure 7. Absorption PCI curves for selected alloy compositions. Solid lines have been added as a guide for the eye.

compositions, TiVZrNbHf, $TiV_{0.5}ZrNbHf$, and TiVZrNb. Notably the TiVZrNbHf phase reaches H/M = 2, and TiVZrNb is at half of that. A number of other compositions were also tried (TiZrNbHf, TiZrHf, TiVNb, and TiVHf), but most showed no major absorption (TiZrNbHf showed absorption at RT when activated at 500 °C, but the equilibrium pressure was very low and within the error of the transducer). The reason for this is unclear but might stem from the very slow hydrogen dosing of the technique compared to the single pulse used in the original synthesis in Figure 2. This, in turn, keeps the alloys at elevated temperatures for much longer, which might cause the alloys to

phase-separate or build up impregnable surface oxides. RT measurements were also attempted, but the equilibrium pressures were below the detectable limits of the instrument.

For the three compositions that gave measurable data, the thermodynamic properties were extracted using the van't Hoff method presented in Figure 8. The enthalpy of absorption
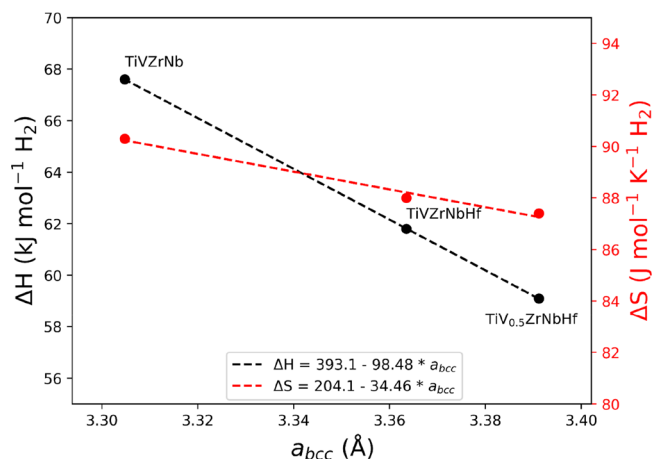

Figure 8. Linear correlations between ΔH_{abs} (black), ΔS_{abs} (red), and unit cell parameters of the selected as-synthesized alloys. The corresponding van't Hoff plots can be found in Figure S9.

follows a linear trend, decreasing with increasing unit cell parameter of the alloy. This trend seems to be inverted to the well-established one for other types of metal hydrides (AB, AB_2, and AB_5), where the increasing size of the interstitial volumes stabilizes the hydride.[35−37] The results in Figure 8 are, however, limited to only three data points and stable metal hydride systems. It is possible that the established trend is recovered with additional data. Considering that the unit cell parameter can be well approximated in HEAs using Vegard's law, a great deal of chemical tunability is possible in order to design HEA-based metal hydrides with different desirable thermodynamics.

Interestingly, the entropy of absorption is rather low (80−90 J/mol·K H_2). This value is often seen as constant around 130 J/mol·K H_2 regardless of the host metal. This surprisingly small change in the entropy of hydrogen in the metal lattice compared to gaseous hydrogen indicates that the hydrogen surroundings are disordered, preferring a mix of nearest-neighbor metals instead of local ordering, in agreement with the findings in ref 23. It is also worth noting that the low value of ΔS can be partially attributed to measurement of the isotherms at high temperature, which will increase the entropy of the gas phase, therefore decreasing ΔS.

■ CONCLUSIONS

A series of ternary, quaternary, and quinary HEAs consisting of the elements Ti, V, Zr, Nb, and Hf have been synthesized and evaluated based on their hydrogen sorption properties. Among the 21 investigated compositions, 17 crystallized in single-phase bcc solid solutions and 1 in a hexagonal structure. Furthermore, 15 of the single-phase alloys produced either fcc or bct metal hydrides with maximum H/M ratios close to 2. Large amounts of Zr and Hf were seen to dictate the formation of bct metal hydrides over fcc. Upon hydrogenation, the unit cell volume expansion per metal atom increases linearly with both VEC and χ_p of the alloys. The hydrogen release mechanisms were found to

be composed of several steps, where the second one decreases in temperature linearly with increasing VEC.

The enthalpy of formation was found to follow a linear trend with regard to the unit cell parameter of the hydrogen-free alloy. This, combined with the great chemical tunability of HEAs, should allow tailoring of the thermodynamic properties toward many different applications of metal hydrides.

All in all, it is shown that HEAs and their respective hydrides exhibit a rather complex relationship between the chemical composition and hydrogen storage properties. However, the findings here corroborate the theory that control over VEC and χ_p is crucial for the design of HEAs for hydrogen storage applications. On the basis of the results presented here and in the literature, it should now soon be possible to design novel alloys with the desired hydrogen storage properties for a specific application.

■ ASSOCIATED CONTENT

ⓈⒾ Supporting Information

The Supporting Information is available free of charge at https://pubs.acs.org/doi/10.1021/acs.inorgchem.0c03270.

     Supporting figures and tables (PDF)

■ AUTHOR INFORMATION

Corresponding Author

Gustav Ek − *Department of Chemistry – Ångström Laboratory, Uppsala University, Uppsala SE-75120, Sweden;* ⓞ orcid.org/0000-0003-4831-3842; Email: gustav.ek@ kemi.uu.se

Authors

Magnus M. Nygård − *Department for Neutron Materials Characterization, Institute for Energy Technology, Kjeller NO-2027, Norway*

Adriano F. Pavan − *Department of Chemistry – Ångström Laboratory, Uppsala University, Uppsala SE-75120, Sweden*

Jorge Montero − *Institut de Chimie et des Matériaux Paris Est, Université de Paris Est, CNRS, UPEC, Thiais 94320, France*

Paul F. Henry − *Department of Chemistry – Ångström Laboratory, Uppsala University, Uppsala SE-75120, Sweden; ISIS Pulsed Neutron and Muon Source, Rutherford Appleton Laboratory, Didcot OX11 0QX, United Kingdom;* ⓞ orcid.org/0000-0003-4714-6587

Magnus H. Sørby − *Department for Neutron Materials Characterization, Institute for Energy Technology, Kjeller NO-2027, Norway*

Matthew Witman − *Sandia National Laboratories, Livermore, California 94551, United States;* ⓞ orcid.org/0000-0001-6263-5114

Vitalie Stavila − *Sandia National Laboratories, Livermore, California 94551, United States;* ⓞ orcid.org/0000-0003-0981-0432

Claudia Zlotea − *Institut de Chimie et des Matériaux Paris Est, Université de Paris Est, CNRS, UPEC, Thiais 94320, France;* ⓞ orcid.org/0000-0002-4454-6991

Bjørn C. Hauback − *Department for Neutron Materials Characterization, Institute for Energy Technology, Kjeller NO-2027, Norway;* ⓞ orcid.org/0000-0002-2717-6941

Martin Sahlberg − *Department of Chemistry – Ångström Laboratory, Uppsala University, Uppsala SE-75120, Sweden*

Complete contact information is available at: https://pubs.acs.org/10.1021/acs.inorgchem.0c03270

Notes

The authors declare no competing financial interest.

■ REFERENCES

(1) Hirscher, M.; Yartys, V. A.; Baricco, M.; Bellosta von Colbe, J.; Blanchard, D.; Bowman, R. C.; Broom, D. P.; Buckley, C. E.; Chang, F.; Chen, P.; et al. Materials for Hydrogen-Based Energy Storage - Past, Recent Progress and Future Outlook. *J. Alloys Compd.* **2020**, *827*, 153548.

(2) Cohen, R. L.; West, K. W.; Wernick, J. H. Degradation of LaNi5 by Temperature-Induced Cycling. *J. Less-Common Met.* **1980**, *73* (2), 273−279.

(3) Joubert, J. M.; Latroche, M.; Percheron-Guégan, A. Hydrogen Absorption Properties of Several Intermetallic Compounds of the ZrNi System. *J. Alloys Compd.* **1995**, *231* (1−2), 494−497.

(4) Schlapbach, L.; Riesterer, T. The Activation of FeTi for Hydrogen Absorption. *Appl. Phys. A: Solids Surf.* **1983**, *32* (4), 169−182.

(5) Yeh, J.-W.; Chen, S.-K.; Lin, S.-J.; Gan, J.-Y.; Chin, T.-S.; Shun, T.-T.; Tsau, C.-H.; Chang, S.-Y. Nanostructured High-Entropy Alloys with Multiple Principal Elements: Novel Alloy Design Concepts and Outcomes. *Adv. Eng. Mater.* **2004**, *6* (5), 299−303.

(6) Miracle, D. B.; Senkov, O. N. A Critical Review of High Entropy Alloys and Related Concepts. *Acta Mater.* **2017**, *122*, 448−511.

(7) Gao, M. C.; Miracle, D. B.; Maurice, D.; Yan, X.; Zhang, Y.; Hawk, J. A. High-Entropy Functional Materials. *J. Mater. Res.* **2018**, *33* (19), 3138−3155.

(8) Kunce, I.; Polański, M.; Czujko, T. Microstructures and Hydrogen Storage Properties of La Ni Fe V Mn Alloys. *Int. J. Hydrogen Energy* **2017**, *42* (44), 27154−27164.

(9) Kunce, I.; Polanski, M.; Bystrzycki, J. Structure and Hydrogen Storage Properties of a High Entropy ZrTiVCrFeNi Alloy Synthesized Using Laser Engineered Net Shaping (LENS). *Int. J. Hydrogen Energy* **2013**, *38* (27), 12180−12189.

(10) Zepon, G.; Leiva, D. R.; Strozi, R. B.; Bedoch, A.; Figueroa, S. J. A.; Ishikawa, T. T.; Botta, W. J. Hydrogen-Induced Phase Transition of MgZrTiFe0.5Co0.5Ni0.5 High Entropy Alloy. *Int. J. Hydrogen Energy* **2018**, *43* (3), 1702−1708.

(11) Montero, J.; Zlotea, C.; Ek, G.; Crivello, J.-C.; Laversenne, L.; Sahlberg, M. TiVZrNb Multi-Principal-Element Alloy: Synthesis Optimization, Structural, and Hydrogen Sorption Properties. *Molecules* **2019**, *24* (15), 2799.

(12) Montero, J.; Ek, G.; Laversenne, L.; Nassif, V.; Zepon, G.; Sahlberg, M.; Zlotea, C. Hydrogen Storage Properties of the Refractory Ti-V-Zr-Nb-Ta Multi-Principal Element Alloy. *J. Alloys Compd.* **2020**, *835*, 155376.

(13) Kunce, I.; Polanski, M.; Bystrzycki, J. Microstructure and Hydrogen Storage Properties of a TiZrNbMoV High Entropy Alloy Synthesized Using Laser Engineered Net Shaping (LENS). *Int. J. Hydrogen Energy* **2014**, *39* (18), 9904−9910.

(14) Sahlberg, M.; Karlsson, D.; Zlotea, C.; Jansson, U. Superior Hydrogen Storage in High Entropy Alloys. *Sci. Rep.* **2016**, *6*, 1−6.

(15) Karlsson, D.; Ek, G.; Cedervall, J.; Zlotea, C.; Møller, K. T.; Hansen, T. C.; Bednarčík, J.; Paskevicius, M.; Sørby, M. H.; Jensen, T. R.; et al. Structure and Hydrogenation Properties of a HfNbTiVZr High-Entropy Alloy. *Inorg. Chem.* **2018**, *57* (4), 2103−2110.

(16) Zlotea, C.; Sow, M. A.; Ek, G.; Couzinié, J.-P.; Perrière, L.; Guillot, I.; Bourgon, J.; Møller, K. T.; Jensen, T. R.; Akiba, E.; Sahlberg, M. Hydrogen Sorption in TiZrNbHfTa High Entropy Alloy. *J. Alloys Compd.* **2019**, *775*, 667.

(17) Nygård, M. M.; Ek, G.; Karlsson, D.; Sahlberg, M.; Sørby, M. H.; Hauback, B. C. Hydrogen Storage in High-Entropy Alloys with Varying Degree of Local Lattice Strain. *Int. J. Hydrogen Energy* **2019**, *44* (55), 29140−29149.

(18) Nygård, M. M.; Ek, G.; Karlsson, D.; Sørby, M. H.; Sahlberg, M.; Hauback, B. C. Counting Electrons - A New Approach to Tailor the Hydrogen Sorption Properties of High-Entropy Alloys. *Acta Mater.* **2019**, *175*, 121−129.

(19) Shen, H.; Zhang, J.; Hu, J.; Zhang, J.; Mao, Y.; Xiao, H.; Zhou, X.; Zu, X. A Novel TiZrHfMoNb High-Entropy Alloy for Solar Thermal Energy Storage. *Nanomaterials* **2019**, *9* (2), 248.

(20) Hu, J.; Shen, H.; Jiang, M.; Gong, H.; Xiao, H.; Liu, Z.; Sun, G.; Zu, X. A DFT Study of Hydrogen Storage in High-Entropy Alloy TiZrHfScMo. *Nanomaterials* **2019**, *9* (3), 461.

(21) Nakamura, K.; Fukai, Y. High-Pressure Studies of High-Concentration Phases of the TiH System. *J. Alloys Compd.* **1995**, *231* (1−2), 46−50.

(22) Fukai, Y. *The Metal−Hydrogen System*; Springer Series in Materials Science; Springer-Verlag: Berlin, 2005; Vol. *21*.

(23) Nygård, M. M.; Sławiński, W. A.; Ek, G.; Sørby, M. H.; Sahlberg, M.; Keen, D. A.; Hauback, B. C. Local Order in High-Entropy Alloys and Associated Deuterides - a Total Scattering and Reverse Monte Carlo Study. *Acta Mater.* **2020**, *199*, 504−513.

(24) Kittel, C. *Introduction to Solid State Physics*, 6th ed.; Wiley, 1986.

(25) Brinks, H. W.; Fossdal, A.; Bowman, R. C.; Hauback, B. C. Pressure-Composition Isotherms of TbNiAlHx. *J. Alloys Compd.* **2006**, *417* (1−2), 92−95.

(26) Rietveld, H. M. A Profile Refinement Method for Nuclear and Magnetic Structures. *J. Appl. Crystallogr.* **1969**, *2* (2), 65−71.

(27) Coelho, A. A. TOPAS and TOPAS-Academic: An Optimization Program Integrating Computer Algebra and Crystallographic Objects Written in C++. *J. Appl. Crystallogr.* **2018**, *51* (1), 210−218.

(28) Smith, R. I.; Hull, S.; Tucker, M. G.; Playford, H. Y.; McPhail, D. J.; Waller, S. P.; Norberg, S. T. The Upgraded Polaris Powder Diffractometer at the ISIS Neutron Source. *Rev. Sci. Instrum.* **2019**, *90* (11), 115101.

(29) Wood, T. J.; Makepeace, J. W.; David, W. I. F. Neutron Diffraction and Gravimetric Study of the Iron Nitriding Reaction under Ammonia Decomposition Conditions. *Phys. Chem. Chem. Phys.* **2017**, *19* (40), 27859−27865.

(30) Gross, K. J.; Carrington, K. R.; Berkeley, C. Recommended Best Practices for the Characterization of Storage Properties of Hydrogen Storage Materials. *Adsorpt. J. Int. Adsorpt. Soc.* **2010**, 1−301.

(31) Singh, P.; Gupta, S.; Thimmaiah, S.; Thoeny, B.; Ray, P. K.; Smirnov, A. V.; Johnson, D. D.; Kramer, M. J. Vacancy-Mediated Complex Phase Selection in High Entropy Alloys. *Acta Mater.* **2020**, *194*, 540−546.

(32) Tracy, C. L.; Park, S.; Rittman, D. R.; Zinkle, S. J.; Bei, H.; Lang, M.; Ewing, R. C.; Mao, W. L. High Pressure Synthesis of a Hexagonal Close-Packed Phase of the High-Entropy Alloy CrMnFeCoNi. *Nat. Commun.* **2017**, *8* (1), 15634.

(33) Qiao, J. W.; Bao, M. L.; Zhao, Y. J.; Yang, H. J.; Wu, Y. C.; Zhang, Y.; Hawk, J. A.; Gao, M. C. Rare-Earth High Entropy Alloys with Hexagonal Close-Packed Structure. *J. Appl. Phys.* **2018**, *124* (19), 195101.

(34) Beavis, L. C. Characteristics of Some Binary Transition Metal Hydrides. *J. Less-Common Met.* **1969**, *19* (4), 315−328.

(35) Lundin, C. E.; Lynch, F. E.; Magee, C. B. A Correlation between the Interstitial Hole Sizes in Intermetallic Compounds and the Thermodynamic Properties of the Hydrides Formed from Those Compounds. *J. Less-Common Met.* **1977**, *56* (1), 19−37.

(36) Fujitani, S.; Yonezu, I.; Saito, T.; Furukawa, N.; Akiba, E.; Hayakawa, H.; Ono, S. Relation between Equilibrium Hydrogen Pressure and Lattice Parameters in Pseudobinary Zr-Mn Alloy Systems. *J. Less-Common Met.* **1991**, *172−174*, 220−230.

(37) Cuevas, F.; Joubert, J.-M.; Latroche, M.; Percheron-Guégan, A. Intermetallic Compounds as Negative Electrodes of Ni/MH Batteries. *Appl. Phys. A: Mater. Sci. Process.* **2001**, *72* (2), 225−238.

(38) Pavan, A. F.; Ek, G.; Henry, P. F.; Sahlberg, M. In-Situ Investigation into the Hydrogen Sorption Pathways of High Entropy Alloy Based Metal Hydrides. *STFC ISIS Neutron Muon Source* **2019**; DOI: 10.5286/ISIS.E.RB1920509.